Development and validation of a virtual aerodynamic model for eVTOVL aircraft

Štěpán Zdobinský[1,*] and *Pavel* Peukert[1]

[1]VÚTS, a.s., Svárovská 619, Liberec XI-R °

Abstract. This paper presents a comprehensive aerodynamic study of a virtual eVTOVL aircraft model, developed through CFD simulations and validated with experimental data. A subscaled ducted fan prototype was tested to compare against simulation outcomes, demonstrating a strong correlation in thrust prediction. Aerodynamic design methods were used to achieve sufficient wing-generated lift during cruise flight, eliminating the need for vertical thrust. Propulsion behavior under critical conditions was analyzed, highlighting the impact of pressure effects, vortex formation, and geometric factors on thrust stability.

1 Introduction

The rapid advancement in electric propulsion for aerial vehicles has led to widespread exploration of VTOL systems, especially in urban environments. Among these, electric vertical take-off and landing aircraft (eVTOVL) (Fig.1) offer unique performance benefits via ducted fan propulsion and thrust vectoring capabilities.

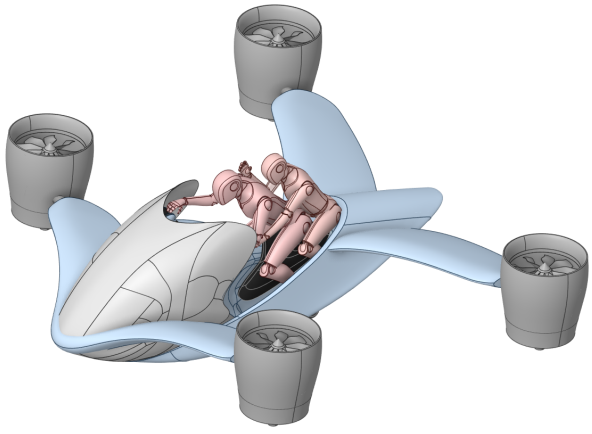

Figure 1. Aircraft eVTOVL.

The studied concept features a tandem-wing layout and four electric ducted fans placed at wing tips. These fans tilt for both vertical lift and forward propulsion, enabling control authority without conventional aerodynamic surfaces. The design aims for a 600 kg MTOW (maximum take off weight) and 230 km/h cruise speed over a 50 km range.

To ensure aerodynamic feasibility, a virtual CFD model was developed and validated against physical measurements using a scaled ducted fan engine. A wing optimization strategy was subsequently applied to generate sufficient lift exclusively through the wings during horizontal flight. Finally, the propulsion system was tested under various configurations and speeds to verify safe thrust generation under all operating conditions.

2 Experimental Methodology and CFD Validation

2.1 Subscaled Ducted Fan Testing

A 1:3 subscale ducted fan model was mounted on a precision dynamometer rig, Fig.2. Thrust was recorded for multiple RPM settings using piezoelectric sensors (KISTLER). The fan's rotational speed was captured via laser tachometry, while current and voltage data were logged using DEWE measuring equipment. Two nacelle configurations were assessed:

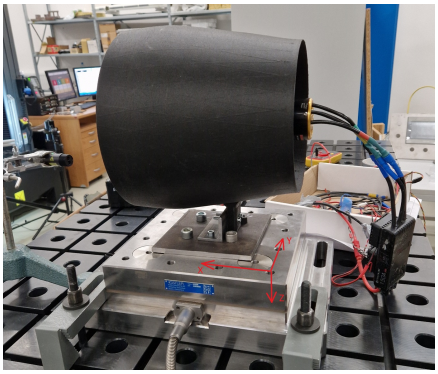

Figure 2. Thrust measurement of the 1:3 subscale electric ducted fan on a dynamometer bench with the long nacelle [1].

*Corresponding author: stepan.zdobinsky@vuts.cz

2.1.1 Analyzed Configuration Overview

The 1:3 subscale ducted-fan model with diameter of 550 mm was studied in two configurations: a "long nacelle" and a "short nacelle." The fan geometry remains identical in both cases; only the axial position of the rotor relative to the housing changes. In the short-nacelle variant, (Figs.3a and 3b).

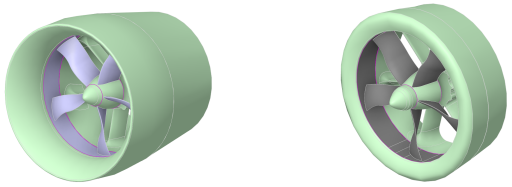

(a) Long nacelle (b) Short nacelle

Figure 3. Geometries of the 1:3 subscale ducted fan with long and short nacelles.

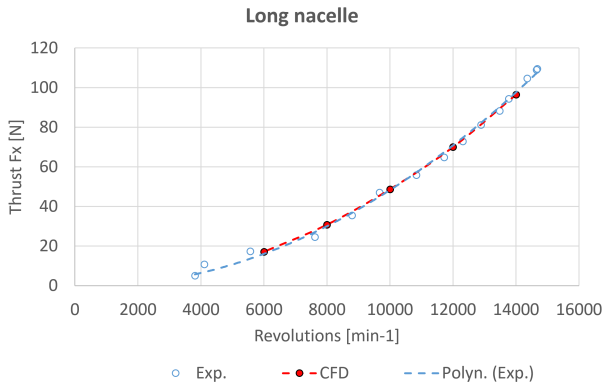

Figure 4. Thrust of the ducted fan with the long nacelle.

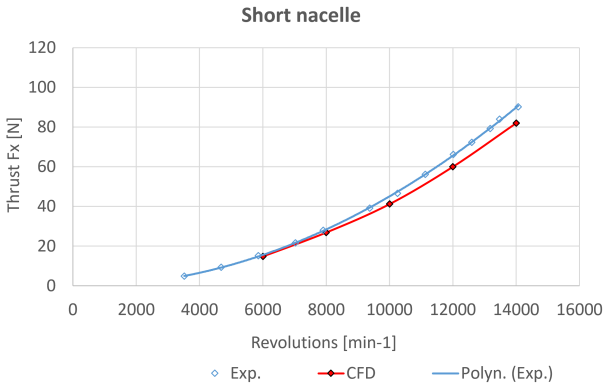

Figure 5. Thrust of the ducted fan with the short nacelle.

Comparing CFD and experiment:

- **Long nacelle:** shows minimal deviation (<1.3%) between simulation and measured thrust, Fig.4.
- **Short nacelle:** exhibits increasing deviation with RPM, peaking at 8.7% due to uncertain rotor positioning in the axis position, Fig.5.

Comparing the two geometries (Fig. 6):

- Measured thrust reduction between long and short nacelle: 8.2%
- CFD prediction: 15.0% reduction
- Prediction error: 6.6%

The results confirm good agreement between numerical simulation and reality, particularly when accurate geometry is available.

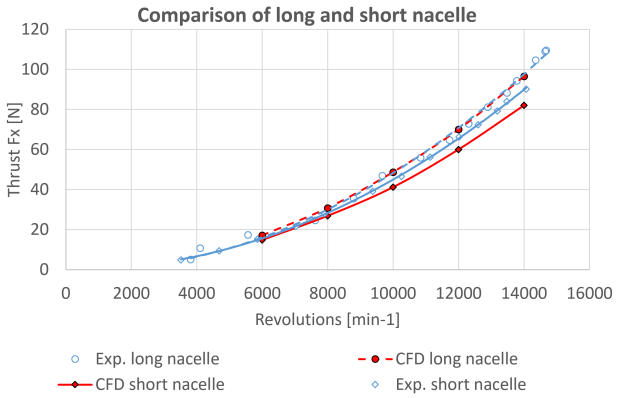

Figure 6. Thrust comparison of the long and short nacelle.

2.2 CFD Simulation of the 1:3 Subscale Electric Ducted Fan Model

2.2.1 Computational Domain and Mesh

The flow domain is bounded by a curved outlet wall designed to accommodate future thrust-vectoring studies (see Fig.7). Boundary conditions are as follows:

- Inlet: `pressure inlet` set to ambient atmospheric pressure.
- Outlet: `pressure outlet` at 101.3 kPa.
- Lateral faces: `symmetry` (zero velocity gradient).

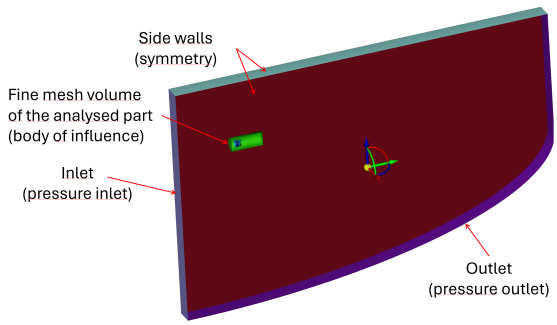

Figure 7. Cross-section of the computational domain.

The mesh comprises approximately 14 million polyhexcore cells:

- Blade surface cell size: 0.05 mm at leading/trailing edges, up to 4 mm on blade faces.

- Nacelle surface: up to 8 mm; body-of-influence region around the rotor: 32 mm; far-field boundaries: 0.5 m.
- Prism layers: 10 layers along all fan and nacelle walls, first-cell height 0.01 mm, growth factor 0.272 (Fig.8.

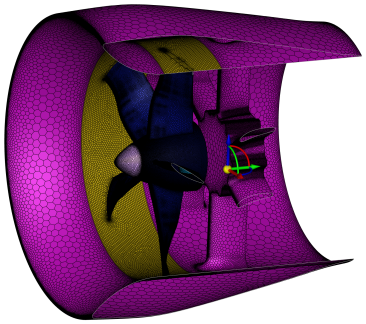

Figure 8. Cross-section of the computational mesh of the 1:3 scale ducted-fan.

2.2.2 Solver Configuration

- Simulation type: steady-state RANS
- Rotor modeling: Multiple Reference Frame (MRF) – "frozen rotor" approach assumes fixed rotating region and imposes rotation in the cell zone surrounding the fan/rotor
- Turbulence model: SST $k-\omega$ (default constants)
- Gas model: ideal gas (`Ideal Gas`); energy equation enabled
- Other solver parameters: left at default settings
- Wall-distance resolution: nondimensional $y^+ \leq 3$ in all critical areas (see Fig. 9)

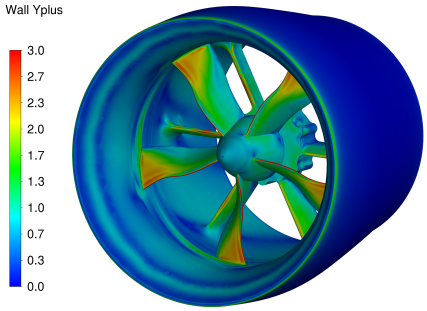

Figure 9. Contours of Wall-distance y+ on the 1:3 scale ducted-fan.

3 Aerodynamic Optimization Using CFD

3.1 Aerodynamic design of lift-increasing measures for a eVTOVL model

Since the propulsion concept is still under development, it was not considered in the initial aerodynamic design of the eVTOVL model. Its impact must be verified through a full simulation in a subsequent project. Another reason for not considering ducted fans is the significant boundary layer separation (Fig.10) observed in the current horizontal flight configuration. This considerably prolonged computation time and reduced accuracy.

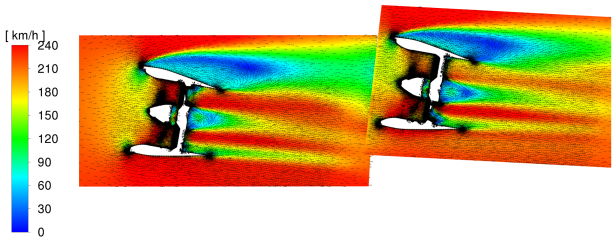

Figure 10. Cross-section through ducted fans with contours of velocity.

The objective of the eVTOVL model's aerodynamic design is to generate sufficient lift at horizontal flight solely through the wings, without the contribution of the vertical thrust from the propulsion system. This enables the engines to be oriented horizontally for the forward flight, using their thrust only to overcome drag, which is an order of magnitude lower than the corresponding lift force. This allows significantly to increase flight range and endurance.

The maximum take-off weight was set to 600 kg, requiring a lift force of 6000 N to be produced by the wings not only at maximum speed, but also at reduced velocities. The aerodynamic measures applied are listed in Table 2. The contribution of each measure was first evaluated at the maximum design speed of 230 km/h. If adequate lift was not achieved under these conditions, lower speeds were disregarded, as aerodynamic force decreases with the square of the airspeed.

3.2 Results

Tab. 1 shows overview of the measures. Tab. 2 summarizes lift and drag at multiple speeds for each applied aerodynamic measure related to the wings.

Table 1. Overview of measures.

Nr.	Measure
1	Dron without engines
2	Straight wings - without sweep and dihedral
3	Windshield and incidence angle of the rear wing from 3° to 8°
4	Incidence angle of of the front wing from 3° to 8°
5	Increase of wing area onto 11,5 m^2 at wingspan of 6 m ($\lambda = 6$)
6	Increase of wingspan onto 8 m at $\lambda = 11$

Aspect ratio λ is defined:

$$\lambda = \frac{l^2}{S}, \tag{1}$$

where is l - wingspan [m] and S - wing area [m^2]

Table 2. Force contributions by each measures.

Nr.	Speed [km/h]	Drag [N]	Lift [N]
1	230	738	1530
2	230	826	1598
3	230	1275	5657
4	230	1401	6286
5	230	2052	13338
	180	1260	8136
	150	887	5580
6	230	2088	19134
	180	1278	11628
	150	882	7992
	135	720	6462
	120	558	5076
	90	320	2808
	60	144	1224

3.3 The main design Changes

Three main design steps were implemented to get sufficient lift force:

- Expand wing area to 11.5 m^2 (the highest lift contribution)
- Extend wingspan to 8 m with aspect ratio $\lambda = 11$ (the second highest lift contribution)
- Increase incidence angle of both wings to 8°

Lift targets for 600 kg MTOW are fulfilled at 135 km/h and above, enabling transition to fully horizontal fan orientation.

Achieving sufficient lift at even lower speeds can be accomplished by further increasing the wingspan or by enhancing the aspect ratio of the wings. However, further increasing the wingspan is no longer desirable due to the need to maintain compactness. Increasing the aspect ratio of the wings could be feasible with respect to the structural strength of the wing.

Fig.11 shows the zero total pressure coefficient of the original model, while Fig.12 presents the model with the new wing configuration.

The isosurface defined by the total pressure coefficient $c_{p_{tot}} = 0$ encloses a region within the total pressure coefficient $c_{p_{tot}} < 0$, indicates a local loss of total pressure relative to the free stream. This typically reflects zones affected by viscous dissipation, flow separation, or turbulence, and may correspond to areas of reduced aerodynamic efficiency or flow instability within the system.

In the next design phase, following the optimization of the fuselage, it is necessary to design aerodynamic transitions between the wings and the fuselage.

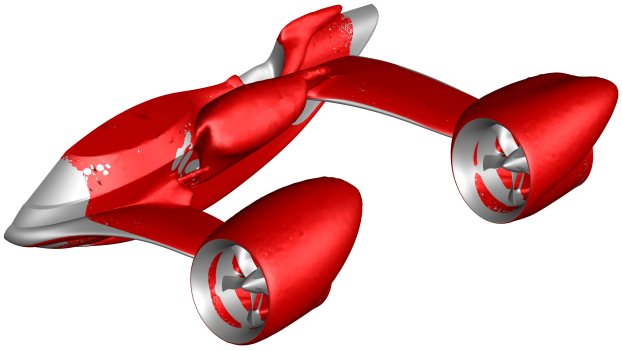

Figure 11. Original dron with iso-surface $\mathbf{c_{p_{tot}}} = 0$.

Figure 12. Dron with optimized wings configuration with iso-surface $\mathbf{c_{p_{tot}}} = 0$.

4 Propulsion System Evaluation

4.1 Analysis of typical and critical operating regimes of the engine

During flight testing of the 1:3 subscale eVTOVL model, it was observed that at forward speeds exceeding 60 km/h, the eVTOVL model suffers from a loss of thrust and controllability. This is due to the absence of aerodynamic control surfaces, with maneuvering carried out solely by tilting the motors.

This phenomenon was simulated and analysed at the most critical speed of 120 km/h, where wing-generated lift remains insufficient, and the airflow is most susceptible to separation at the sharp edges of the motor inlets.

Table 3 presents the influence of flight speed, motor tilt angle, and rotational speed on the thrust produced by the 1:3 scale ducted fan model. The baseline configuration for both variants (long and short nacelle) assumes zero forward velocity (motor stationary) and a tilt angle of 0° (horizontal orientation). Two motor regimes were selected: the

region of maximum continuous RPM at 12000 rpm and a 50% power regime at 6000 rpm.

Table 3. Effect of speed, ducted fan tilt, and rotational speed on the thrust of the 1:3 subscale fan model.

Nacelle	Speed [km/h]	Ducted fan tilt [deg]	RPM [ot/min]	Thrust [N]
Long	0	0	12000	70
	120	-"-	-"-	34
	-"-	85	-"-	47
-"-	0	0	6000	17
	120	-"-	-"-	4,4
	-"-	85	-"-	6,5
short	0	0	12000	60
	120	-"-	-"-	30
	-"-	85	-"-	49
-"-	0	0	6000	14,9
	120	-"-	-"-	10
	-"-	85	-"-	16,2

The expected decrease in thrust at higher speeds was confirmed, consistent with the law of momentum conservation.

4.2 Pressure and Flow Analysis

Interestingly, at 6000 rpm and a speed of 120 km/h, the long nacelle produced a significantly lower thrust by 6.6 N (56%) while at static conditions, it generated 10 N (14%) more thrust than the short nacelle.

Fig.13 and 14 reveal the reason behind this phenomenon: in the intake area of the long nacelle, static pressure increases, resulting in reduced thrust. This phenomenon can be mitigated by installing anti-surge flaps in front of the rotor. The pressure difference between the nacelle interior and exterior causes the flaps to open autonomously, relieving the excess pressure at the fan inlet.

Another notable finding from Table 3 is the influence of motor tilt on thrust. At a tilt angle of 85° and a speed of 120 km/h, the thrust was higher across both configurations and motor regimes compared to the forward-facing orientation. However, this position induces strong vortex structures at the inlet. Under real-world conditions, such vortices form in a non-stationary manner and pose a risk of complete thrust loss.

4.3 Effect of the nacelle length during motor tilt on thrust performance

Fig.15 and 16 illustrate how the nacelle length affects flow at a 85° tilt in full-power (12000 rpm) and half-power (6000 rpm) modes. At lower RPM, flow separation occurs more readily, especially in the long nacelle, where thrust drops by 60% compared to the short nacelle. Conversely, the short nacelle under full power shows an almost uniform velocity field.

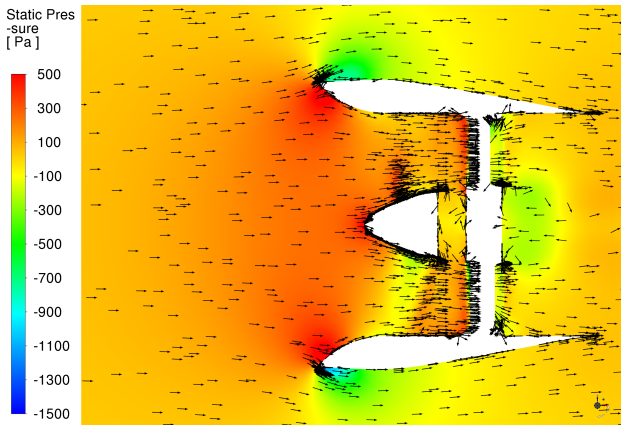

Figure 13. Contours of the static pressure flow field in a cross-section of the ducted fan with a long nacelle.

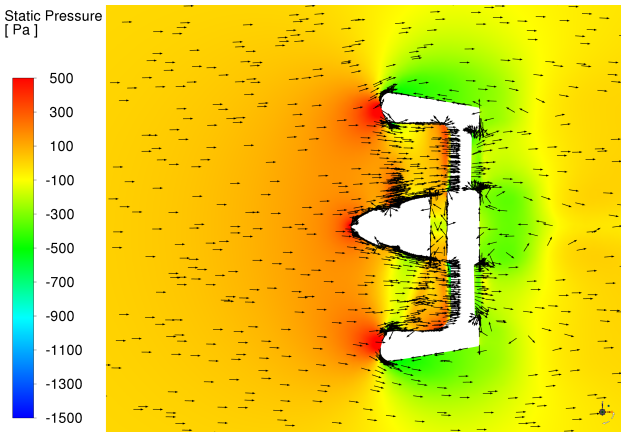

Figure 14. Contours of the static pressure flow field in a cross-section of the ducted fan with a short nacelle.

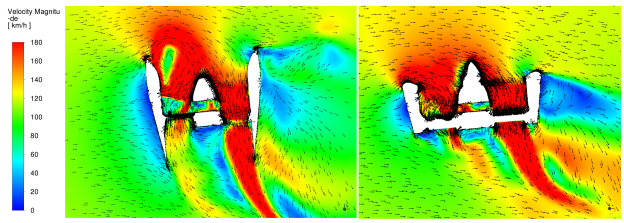

Figure 15. Contours of the velocity flow field in a cross-section of the ducted fan at 12000 rpm and horizontal speed of 120 km/h with long and short nacelles.

5 Conclusion and Future Recommendations

5.1 Conclusion of Data Measurement and Analysis for Comparison of Virtual and Real Product

The objective of this work was to validate the numerical simulation by means of experiment. Static thrust measurements were carried out on a horizontally mounted motor fixed to a dynamometer. Thrust was recorded as a function of rotational speed (RPM). Two configurations were

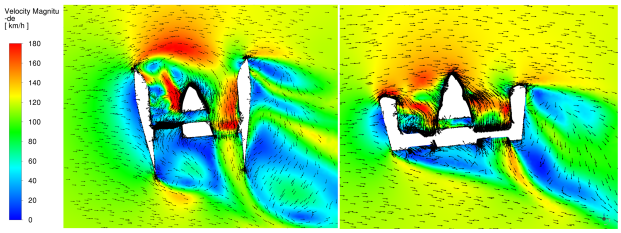

Figure 16. Contours of velocity flow field in a cross-section of the ducted fan at 6000 rpm and horizontal speed of 120 km/h with long and short nacelles.

tested: one with a short motor cover (nacelle) and another with a long one.

When the full geometry of the long nacelle configuration was provided, the simulation closely matched the experimental measurements across the entire RPM range. At 14,000 rpm, the simulation deviated from the measured value by only 1.3 N (1.3%), as shown in Fig.4.

In contrast, the short nacelle configuration showed a simulation error of 7.9 N (8.7%) at the same RPM. The greater deviation was caused by inaccurate axial placement of the fan within the nacelle geometry (between the model and the real subscale) due to the absence of precise digital positioning, as shown in Fig.5.

When analyzing the effect of shortening the nacelle, the experiment recorded an 8.2% reduction in thrust, while the simulation predicted a decrease of 15.0%, as shown in Fig.6. The discrepancy between simulated and measured values was 6.5 N (6.6%).

Therefore, when component placement is precisely defined, the CFD simulation shows strong agreement with experimental data and can be reliably used for further aerodynamic analysis.

5.2 Conclusion of Virtual eVTOVL Model Development and Physical Product Evaluation

To reduce computational demands, aerodynamic optimization measures aimed at increasing lift were conducted on a 1:3 scale drone model. This model was also used for early flight testing and ongoing development.

The goal was to identify aerodynamic solutions that preserve drone compactness while enabling sufficient lift through the wings, without relying on engine-generated vertical thrust. Three key design modifications were successfully implemented, allowing adequate lift generation at speeds above 135 km/h without motor contribution.

These included:

- Increasing the incidence angle of both front and rear wings from 3° to 8°
- Increasing total wing area from 3 m² to 11.5 m²
- Increasing wing aspect ratio from 6 to 11 (corresponding to a wingspan expansion from 6 m to 8 m at constant wing area)

Additionally, the eVTOLV model's propulsion concept using tilting motors that also provide control was evaluated. Flight tests on the scaled model revealed controllability issues above 60 km/h. This phenomenon was analyzed using the same 1:3 subscale fan model as in the validation tests.

The most critical condition was identified at 120 km/h forward speed, where wing lift remained insufficient and flow separation occurred at sharp motor intake edges.

At 120 km/h and 50% thrust power, the long nacelle configuration delivered 56% less thrust than its short counterpart, reversing the trend observed under static conditions. The reason is the increase in static air pressure in the motor intake area.

Another notable observation was that at a ducted fan tilt angle of 85°, thrust was higher than in the forward-facing direction at 120 km/h. This can be explained by the law of momentum conservation: thrust depends on the acceleration of mass flow. In forward orientation, incoming air already possesses velocity, limiting acceleration. In contrast, when flow enters perpendicularly, acceleration and thus thrust is greater.

However, ducted fan tilt also introduced strong vortex structures at the intake. At full power, these vortices disappeared in the short nacelle configuration. In the long nacelle at 50% power, flow separation was most severe. Importantly, such vortex formation is non-stationary in reality and may lead to complete airflow disruption—even in the short nacelle variant.

In summary, the long nacelle offers advantages only under static conditions. With increasing forward speed and reduced RPM, this advantage diminishes rapidly and even becomes a disadvantage. The short nacelle substantially outperforms its counterpart—especially under tilt and at 50% thrust settings.

Acknowledgement

This publication was supported by the Czech Ministry of Industry and Trade in the framework of the institutional support for long-term conceptual development of research organization - recipient VÚTS, a.s.

References

[1] N. Palasovics, *Measurement Report: Properties of the Propulsion Motor for Flying Drone*, MER-V-01/2025.